Journal of Materials Chemistry A

ROYAL SOCIETY OF CHEMISTRY

PAPER

View Article Online
View Journal | View Issue

Cite this: J. Mater. Chem. A, 2023, 11, 16626

N and S co-doped nanosheet-like porous carbon derived from sorghum biomass: mechanical nanoarchitecturing for upgraded potassium ion batteries†

Minjun Kim,‡[a] Liang Ma,‡[b] Zhibin Li,[b] Wenjie Mai,[b] Nasim Amiralian,*[a] Alan E. Rowan,[a] Yusuke Yamauchi,[ac] Aimiao Qin,[d] Rana Arslan Afzal,[e] Darren Martin,[e] Ashok Kumar Nanjundan[e] and Jinliang Li*[b]

Received 31st May 2023
Accepted 16th June 2023

DOI: 10.1039/d3ta03215a

rsc.li/materials-a

In this study, nanosheet-like sorghum biomass is obtained by a mild alkaline treatment and high-energy ball milling. N, S co-doped hard carbon (NSSC) with the nanosheet morphology is subsequently synthesized by a direct-carbonization of the nanosheet-like sorghum biomass mixed with thiourea. NSSCs obtained at various annealing temperatures demonstrate that the optimal annealing temperature is necessary to balance the efficient heteroatom-doping and the level of carbonization. NSSC-600 obtained at the optimized annealing temperature of 600 °C presents a great K-ion storage performance as an anode material with a high reversible specific capacity of 268 mA h g^{-1} at 100 mA g^{-1} and outstanding stability over 2400 cycles. The effect of N and S heteroatom-doping on K-ion adsorption capacity is also verified by density functional theory (DFT) calculations.

Introduction

As the global energy demand continues to increase, the development of advanced energy storage systems has become the major focus of research over the past few decades. Currently, the Li-ion battery (LIB) stands as the dominant choice due to its high energy density and long cycle life.[1–4] With the advance of renewable energy technologies and the continuous rise in the cost of lithium, the scope of research has outreached to substitute lithium with cheaper and more abundant alkali metal species such as sodium (Na) and potassium (K).[5–7] With K being a highly abundant resource, K-ion batteries (KIBs) have attracted extensive attention and are considered a promising solution for large-scale energy storage systems to afford the increasing energy demand.[8–10] Moreover, the current knowledge and technologies of LIBs also help to spur the development of KIBs since K undergoes a similar energy-storage mechanisms to Li. Indeed, many anode materials for KIBs are inspired by the preceding development and application of anodes in LIBs.[11,12] The differences in physical and chemical properties between K (larger ionic radius of 1.38 Å and higher electrochemical redox potential of −2.93 V *vs.* SHE) and Li (ionic radius of 0.76 Å and electrochemical redox potential of −3.04 V *vs.* SHE), however, render the conventional anode materials in LIBs incompatible in KIBs.[13–15] The development of a novel anode material of KIBs with high performance and low cost is, therefore, necessary to ideally replace the current state-of-the-art LIB. Although various anode materials for KIBs, such as metals, oxides, sulfides, and other materials have been developed, carbon materials stand out as an ideal candidate.[16–21] However, carbon materials alone are not sufficient to provide the necessary capacity for KIBs, thus resulting in the active study of heteroatom-doped carbon materials for KIBs. For instance, Cao *et al.* reported the synthesis of N, S co-doped carbon nanosheets using ethylene glycol-assisted Sb_2S_3 templates, providing effective channels for rapid ion/electron transmission and achieving high-performance KIBs.[22] Alternatively, Ma *et al.* used sodium polyacrylate as a carbon precursor with a sodium chloride template to prepare N, S co-doped porous carbon, which enhanced electronic conductivity, hence improving K-ion intercalation.[23] N, S co-doped graphene

[a]Australian Institute for Bioengineering and Nanotechnology (AIBN), The University of Queensland, Brisbane, QLD 4072, Australia

[b]Siyuan Laboratory, Guangdong Provincial Engineering Technology Research Center of Vacuum Coating Technologies and New Materials, Guangdong Provincial Key Laboratory of Nanophotonic Manipulation, Department of Physics, Jinan University, Guangzhou 510632, China

[c]Department of Materials Science and Engineering, School of Engineering, Nagoya University, Furo-cho, Chikusa-ku, Nagoya 464-8601, Japan

[d]Key Lab New Processing Technology for Nonferrous Metals & Materials Ministry of Education, College of Materials Science and Engineering, Guilin University of Technology, Guilin 541004, Guangxi, China

[e]School of Chemical Engineering, Faculty of Engineering, Architecture and Information Technology (EAIT), The University of Queensland, Brisbane, Queensland 4072, Australia

† Electronic supplementary information (ESI) available. See DOI: https://doi.org/10.1039/d3ta03215a

‡ These authors contributed equally.

nanosheets synthesized with F127, melamine, and cyanuric acid also demonstrated significantly improved cycling and rate performance for KIBs, which was attributed to increased K-ion adsorption by edge defects formed through co-doping.[24] Although the above-mentioned heteroatom-doped carbon materials show a significant improvement in performance, the source of their precursors is limited in terms of price and availability and the synthetic methods are difficult to achieve large-scale production. Biomass-derived carbons, therefore, have become one of the most preferred choices due to their wide availability and low cost.[25–27] For instance, graphitic N-doped hard carbons derived from corn stalk cores demonstrated a capacity of 176 mA h g^{-1} after 260 cycles at 1 A g^{-1} as the anode material in KIBs.[28] Alternatively, hard carbons derived from potatoes could also deliver a capacity of 152 mA h g^{-1} at 1 A g^{-1} as the anode material in KIBs.[29] Utilizing crop wastes as carbon precursors to obtain anode materials, in turn, leads to effective waste recycling to mitigate potential environmental pollution.[30] Nonetheless, biomass-derived hard carbons obtained by a one-step pyrolysis method often suffer from a low electrical conductivity and a low density of active sites. In this sense, the strategic designing of high-performance biomass-derived hard carbon is of great interest, hence requiring an in-depth investigation. Furthermore, as heteroatom doping is known to significantly improve electrochemical performance by offering additional redox-active sites and improving wettability and electrical conductivity, it is often applied to further improve the energy-storage performance of biomass-derived hard carbon materials.[31–33]

In this work, sorghum biomass was utilized as a precursor to obtain a hard carbon anode material for KIBs. Prior to the direct carbonization, the sorghum biomass was first subjected to delignification and high-energy ball milling (HEBM) to achieve a unique nanosheet-like morphology. Along with the morphological modifications, the modification of the surface chemistry of the nanosheet-like sorghum was achieved by heteroatom-doping. Typically, thiourea was adopted as a source of N and S atoms and mixed with the nanosheet-like sorghum prior to the pyrolysis. During the pyrolysis, thiourea was decomposed to release N and S atoms to the carbon matrix, hence resulting in N, S co-doped hard carbon (NSSC). A range of annealing temperatures (from 400 to 1000 °C) was attempted to understand the effect of annealing temperatures on the level of carbonization and heteroatom-doping. The results demonstrate that the annealing temperature of above 400 °C is essential to achieve a sufficient degree of carbonization to serve as an electrode material while there is an insignificant effect of annealing temperature on the level of heteroatom-doping. As compared to the pristine sorghum-derived hard carbon (SC) obtained without thiourea mixing, the NSSC demonstrates a great enhancement of K-ion storage performance after the annealing temperature optimization. The optimized NSSC-600 presents a high reversible specific capacity of 268 mA h g^{-1} at 100 mA g^{-1} and a high reversible specific capacity of 90 mA h g^{-1} at a high current density of 2 A g^{-1}. Moreover, it demonstrates ultra-stable K-ion storage by maintaining a reversible specific capacity of 110 mA h g^{-1} at 1 A g^{-1} over 2400 cycles. To confirm the electrochemical enhancement mechanism of our NSSC, we conducted the density functional theory (DFT) calculation. It reveals that the N, S co-doping in hard carbon can enhance the electronic structure and make the adsorption of K-ions thermodynamically more favorable, hence achieving significant improvement of performance in KIBs.

Experimental

Materials and methods

Sorghum biomass growth, separation, washing, drying, and grinding Sugargraze™ sorghum seeds, provided by the Department of Agriculture and Fisheries (DAF) of Queensland, were planted and harvested for research purposes. Typically, the upper stem of sorghum (stem part which is at least 1 meter above the ground) was selected as the source of the carbon precursor. The upper stem section of the sorghum was cut into small pieces (~5 cm in length). The sorghum samples were washed three times for about 30 minutes with deionized water at 80 °C, followed by drying at ~55 °C for 3 days in an air-forced oven. The dried sample was ground with an SM 300 Retsch cutting mill and dried in a vacuum at 50 °C for 24 h.

Delignification of sorghum biomass

The dried sorghum sample was stirred in deionized water at 50 °C overnight. While stirring and heating the mixture at 80 °C, 2 wt/vol% of sodium hydroxide solution (NaOH pellets with 98% purity from Chem-Supply) was slowly added to delignify the sorghum sample for 2 h (Fig. 1a). Afterward, the resulting pulp was washed with deionized water and filtered until the effluent became neutral. The pulp was stored in a sealed container.

Pulp mechanical fibrillation

The delignified pulp was diluted with deionized water to make a 0.3 wt% dispersion solution. Before high-energy ball milling treatment (HEBM), the dispersion of delignified pulp was stirred overnight (Fig. 1a). HEBM treatment was performed using a LabStar laboratory agitator bead mill (Netzch, Germany). A 0.2 mm filter mesh was used with 0.4 mm zirconium oxide beads (ZetaBeads® Plus, Netzch, Germany). The initial speed of milling was 1500 rpm for approximately 10 min, reduced by 70 rpm every 2 min until reaching 1000 rpm. After the completion of HEBM treatment, the resultant slurry was freeze-dried.

Preparation of SC and NSSC-*x* (where *x* denotes the applied annealing temperature)

Prior to the carbonization, 0.5 g dried delignified sorghum plant precursor was mixed with 0.5 g thiourea in a corundum boat and then transferred into a tube furnace under a flowing argon atmosphere of 50 mL min^{-1}. Subsequently, the mixture was heat-treated at different temperatures of 400, 600, 800, and 1000 °C with a heating rate of 5 °C min^{-1} to obtain NSSC-400, NSSC-600, NSSC-800 and NSSC-1000, respectively (Fig. 1a). The sorghum-derived carbon without doping, denoted as SC, was synthesized by the same procedure without the addition of thiourea and carbonization at 800 °C.

Characterization

Field-emission scanning electron microscopy (FESEM) was performed using a Zeiss Ultra 55. Transmission electron microscopy (TEM) and high-resolution TEM (HRTEM) were performed using a JEOL-2100F. The structure information was recorded by Raman spectroscopy (Horiba T64000) with 532 nm laser radiation and X-ray diffraction (XRD, Rigaku) with Cu Kα radiation. The surface properties were recorded by Fourier-transform infrared spectroscopy (FTIR, NEXUS 670) using a Nicolet Fourier-transform infrared spectrometer and X-ray photoelectron spectroscopy (XPS) performed using an image photoelectron spectrometer (Thermo Fisher Scientific K-Alpha) with the Al Kα X-ray source. The Brunauer–Emmett–Teller (BET) measurement was performed using a nitrogen adsorption apparatus (Biaode-Kubo×1000) at 77 K. The CHNS elemental analysis was performed using an elemental analyser (Elementar-Vario Micro Cube).

Electrochemical measurement

Typically, 80% active material, 10% Super P carbon black, and 10% carboxymethyl cellulose were mixed in deionized water to prepare a dispersion ink solution. The ink solution was then used to coat the coarse Cu foil. After the ink is completely dried at 100 °C in a vacuum oven, the coated Cu foil was cut into discs with a diameter of 14 mm. The electrodes were packaged into the CR2032-type KIBs in a glovebox (Etelux) fully filled with argon. In the KIB, metallic K foil acted as a counter electrode, and the fiber filter (Whatman) served as a separator. 0.1 mL of 1 M potassium bis(fluorosulfonyl)imide in a mixed solvent of ethylene carbonate/propylene carbonate (volume ratio of 1 : 1) was used as the electrolyte in the battery. The galvanostatic charge–discharge (GCD) curves, and rate and cycle performances were measured using a Neware battery testing system (BTS-4000). The cyclic voltammetry (CV) measurement was performed using a Chenhua electrochemical workstation (C1030) at a scan rate of 0.2 mV s^{-1} unless otherwise noted. The electrochemical impedance spectroscopy (EIS) was performed using a Princeton electrochemical workstation (Veras STAT3-400) with a frequency from 0.1 Hz to 100 kHz.

Density functional theory (DFT) calculations

Our theoretical calculations are based on DFT, and the Baker (PBE) function and the projector enhanced wave (PAW) scheme are used for geometric optimization, which are implemented in the Vienna *ab initio* simulation package (VASP). The adsorption energy (ΔE_a) is defined using the following equation: $\Delta E_a = E_2 - E_1 - \mu_K$, where E_1 is the energy of the system before adsorbing Na ions, E_2 is the total energy of the system after adsorbing K-ions, and μ_K is the chemical potential of a single K atom.

Results and discussion

NSSC-*x* were prepared according to the steps described in Fig. 1a. The sorghum sample was initially washed with deionized water, then delignified with an alkaline solution (2 wt/vol% NaOH) (Fig. S1†). The delignified sorghum was subsequently subjected to HEBM treatment, and finally freezed-dried to obtain the nanosheet-like morphology. Unlike the water-treated sorghum whose lignocellulosic microfibrils remain largely intact (Fig. 1b), significant opening and loosening of the microfibrils are observed in the delignified sorghum (Fig. 1c). The disruption of microfibrils in the delignified sorghum can be attributed to the breaking of chemical bonds between lignocellulosic components (cellulose, hemicellulose and lignin) under alkaline conditions. The following mechanical treatment of delignified sorghum by HEBM successfully generates the nanosheet-like morphology (Fig. 1d). Upon thermal annealing of the nanosheet-like sorghum at a set of different temperatures, NSSC-*x* were obtained (where *x* denotes the applied annealing temperature).

The enlarged FESEM images clearly demonstrate the morphological changes induced by the chemical and mechanical treatments (Fig. 1e–g). To gain further understanding of the effect of each treatment, XRD patterns of the three sorghum samples were obtained. Typically, cellulose has a crystalline phase, whereas lignin and hemicellulose are amorphous. In the XRD spectra of water-treated, delignified and nanosheet-like sorghums, obvious crystalline peaks are detected at 16°, 22° and 34°, which correspond to the $(1\bar{1}0)$, (200), and (004) lattice planes of cellulose I (Fig. 1h). For the delignified sorghum, the peak corresponding to the amorphous cellulose peak at around 18.5° becomes substantially attenuated as compared to water-treated sorghum, indicating that the alkaline treatment successfully removes the amorphous or disordered phase of cellulose in the sorghum (Fig. 1h).[27,34,35] Consequently, the crystallinity index (CrI) of the sorghum samples increases from 42 to 65 after the alkaline treatment. As CrI quantifies the level of the orderliness of cellulose, it demonstrates that non-cellulosic components (lignins, hemicellulose, and impurities) can be successfully removed by the alkaline treatment. From the XRD pattern and CrI value of the nanosheet-like sorghum, no obvious change in the crystallinity is identified after mechanical fibrillation as compared to that of the delignified sorghum sample (Fig. 1h). Next, the change in the functional groups of the sorghum samples by each treatment is investigated by ATR-FTIR. Based on ATR-FTIR spectra, significant decreases in the intensity of the peaks at 1734 cm^{-1} (C=O stretching) and 1511 cm^{-1} (C=C stretching) are observed after the alkaline treatment (Fig. 1i). This decrease in the peak intensity at 1734 cm^{-1} is associated with the breakdown of ester linkages of carboxylic groups of lignin and/or hemicellulose and oxidation of the terminal glucopyranose unit during the delignification process. As the peak at 1511 cm^{-1} corresponds to the C=C stretching vibration of the aromatic ring in lignin, the decreasing peak also results from the process of delignification. The peak at around 1240 cm^{-1} is related to the axial asymmetries of =C–O– in the ether, ester, and phenol groups of lignin, and its intensity also decreases after the delignification. A decrease in the intensity of the peak at 817 cm^{-1} (C–H out of plane bending) is also identified after the delignification process, indicating that the contents of lignin and hemicellulose have been substantially reduced in the delignified sorghum (Fig. 1i). The trend of the spectrum matches well

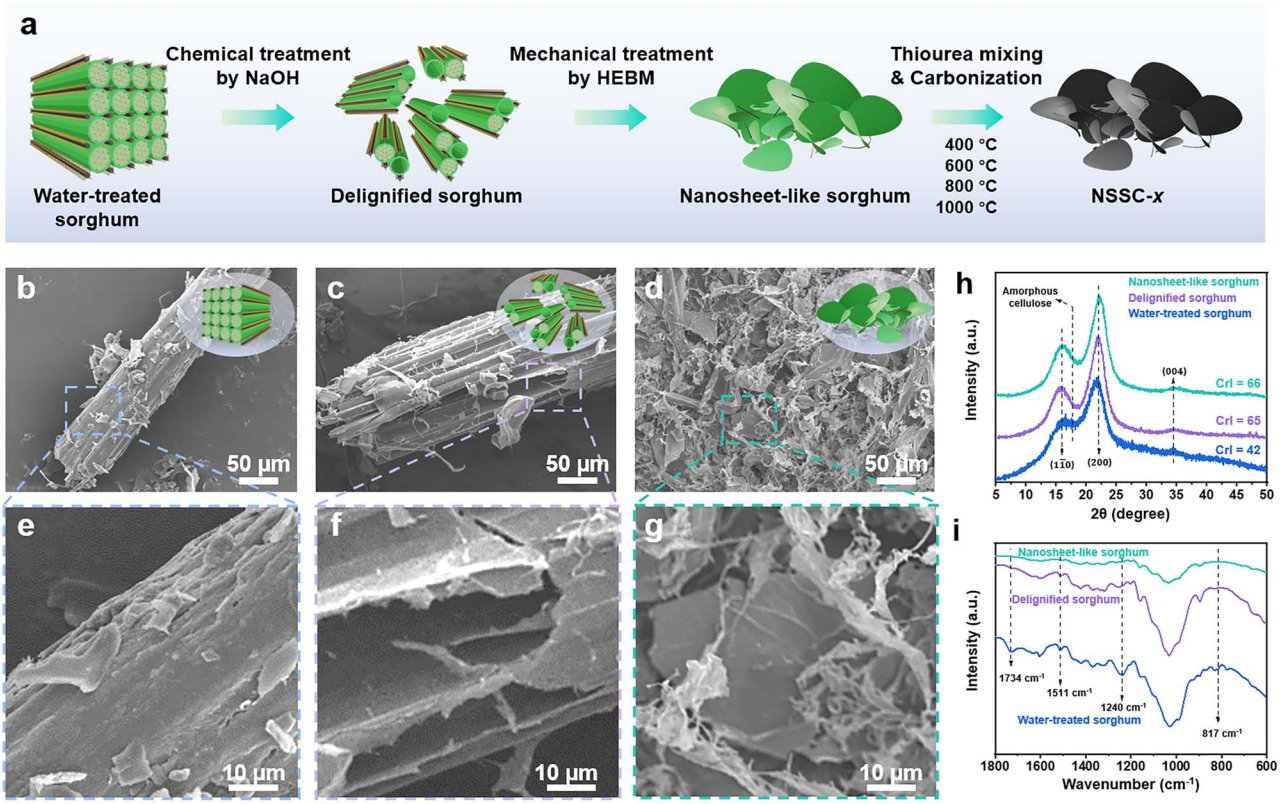

Fig. 1 (a) Description of the synthesis of NSSC-*x*. FESEM images of (b) water-treated sorghum, (c) delignified sorghum, and (d) nanosheet-like sorghum. Enlarged FESEM images of (e) water-treated sorghum, (f) delignified sorghum, and (g) nanosheet-like sorghum. (h) XRD and (i) ATR-FTIR spectra of sorghum samples at each stage of treatment.

between the delignified and the nanosheet-like sorghum, indicating that the additional mechanical treatment does not exert significant influence on the functional groups of sorghum (Fig. 1i).

As the nanosheet-like morphology is highly desirable for the carbon precursor to maximize the contact surface area, the nanosheet-like sorghum was subjected to the subsequent carbonization process. Prior to the carbonization, it was mixed well with thiourea which serves as the source of additional N and S atoms. During the thermal treatment, thiourea molecules undergo thermal decomposition to introduce N and S atoms to the carbon matrix, hence successfully giving rise to NSSC-*x*.[36,37] As observed in the FESEM images, SC and NSSC-*x* demonstrate the typical nanosheet-like morphology (Fig. 2a, b and S2†). The status of co-doping with N and S is verified by the elemental mapping of NSSC-600 (Fig. 2c). The elemental mapping images for C, N, and S atoms show that they are homogeneously distributed throughout NSSC-600, hence confirming the successful co-doping of N and S in the carbon matrix. The HRTEM image of NSSC-600 demonstrates the large interlayer space of 0.38 nm, which potentially promotes the efficient insertion of K-ions (Fig. 2d).[38] In addition, the twisty lattice fringe in NSSC-600 demonstrates a highly disordered structure, which can provide the void for the accommodation of the K cluster during the K-ion (de)intercalation processes.[39]

Next, the XRD spectra of the carbon samples were obtained to investigate their crystalline phase (Fig. 2e). Both spectra present a broad diffraction peak at ~26°, corresponding to the (002) lattice plane of graphitic carbon, indicating that they are highly amorphous carbon in nature.[40,41] To further analyze their chemical bonding, Raman spectra of SC and NSSC-*x* are also provided (Fig. 2f). The Raman spectra show a distinct D band (~1330 cm^{-1}) representing the disordered/partially ordered carbon structure, and a G band (~1575 cm^{-1}) representing graphitized carbon structures, respectively.[42,43] The intensity ratio between D and G bands (I_D/I_G) of carbon materials, therefore, indicates the degree of graphitization which is an important parameter contributing to the electrical conductivity of the carbon.[44] According to the I_D/I_G value, the degree of disorder in the carbon structure is much higher in NSSC-*x* (I_D/I_G between 0.97 and 1.01) as compared to SC (I_D/I_G = 0.87), indicating that the level of defect sites in the carbon increases with the N, S co-doping. Among NSSC-*x*, NSSC-400 typically demonstrates the lowest I_D/I_G value of 0.97. We can attribute such low I_D/I_G value of NSSC-400 to sp^2 vibration of the aromatic rings of the partially decomposed lignin component at a low carbonization temperature of 400 °C. In addition, the mixed thiourea is not likely to undergo complete decomposition when pyrolyzed at 400 °C, hence potentially leading to a lower level of N, S co-doping in carbon and fewer defect sites created in NSSC-400. The increased level of defect sites in NSSC-*x* obtained at or

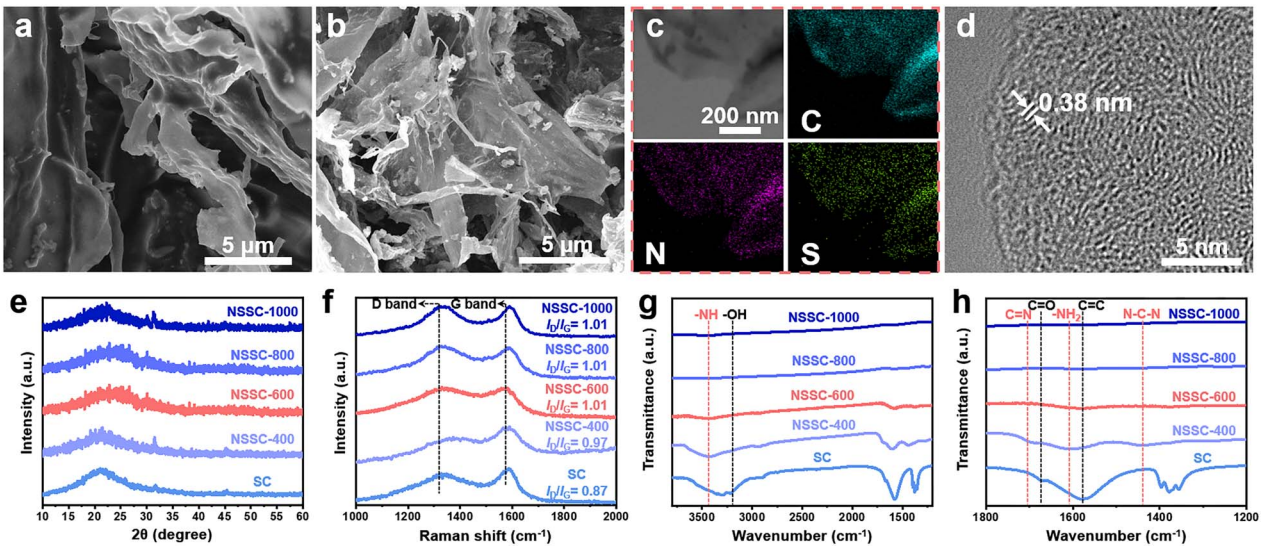

Fig. 2 FESEM image of (a) SC and (b) NSSC-600. (c) Elemental mapping for C, N, and S and (d) HRTEM images of NSSC-600. (e) XRD, (f) Raman spectra and (g and h) FTIR spectra of SC, NSSC-400, NSSC-600, NSSC, and NSSC-1000. Note: as the carbon precursor is derived from the natural sugarcane biomass, potential impurities were identified in the XRD spectra.

above 600 °C is expected to provide more voids in the microstructure to accommodate the K cluster more efficiently, hence contributing to the overall enhancement of K-ion storage.[45] Fig. 2g and h show the FTIR spectra of SC and NSSC-*x*. As compared to SC, NSSC-*x* presents much attenuated or no obvious peaks for C=C, C=O, and –OH peaks at 1578, 1680, and 3440 cm^{-1}, respectively, indicating that N and S co-doping contributes to the increased level of thermal reduction on the surface of NSSC-*x*. In the FTIR spectrum of NSSC-400, four distinct peaks are identified. The peaks at 3440, 1690, 1605, and 1450 cm^{-1} correspond to –NH stretching vibration, C=N stretching, $-NH_2$ bending, and N–C–N stretching vibration, respectively, of the decomposing thiourea in the sample.[46,47] In contrast, the four peaks disappear from the FTIR spectra of NSSC-*x* carbonized at temperatures above 600 °C as thiourea becomes fully decomposed at such high temperatures.[48] Next, the nitrogen adsorption–desorption isotherms of SC and NSSC-600 were obtained to understand their specific surface area and porosity (Fig. S3†). Based on the BET method, the specific surface area of SC is calculated to be 272 $m^2\ g^{-1}$, whereas NSSC-600 only possesses a specific surface area of 21 $m^2\ g^{-1}$. A significant decrease in the specific surface area in NSSC-600 can be attributed to the potential collapse of its porous structure during S and N co-doping at the high annealing temperature. In addition, small sulfur molecules can be formed and confined within the nanopores of NSSC-600, hence also contributing to the decrease in the specific surface area.[49–51]

To confirm the content of S element in our samples, we conducted the CHNS measurement and found that the S content in NSSC-400, NSSC-600, NSSC-800, and NSSC-1000 is 0.96, 1.62, 1.23, and 1.41at%, respectively (Table S1†). It demonstrates that there is an insignificant effect of pyrolysis temperature on the sulfur content of our carbon samples. The surface chemistry of SC and NSSC-600 was then investigated by XPS analysis. Typically, N 1s and S 2p peaks are present in the survey XPS spectrum of NSSC-600, indicating that the N and S are doped in the carbon matrix (Fig. S4a†). In contrast, the S 2p peak is absent in the survey XPS spectrum of SC (Fig. S4a†). Based on the survey XPS spectrum, the relative contents of N and S are 4.6 and 1.1 at% for NSSC-600. To further understand the surface chemistry of these samples, we obtained their high-resolution XPS spectra for C 1s (Fig. 3a and S4b†). As compared to SC, the intensity of peak at 286.2 eV increases in NSSC-600 because of the formation of C–S and C–N bonds.[32,52] Fig. 3b shows the high-resolution XPS spectrum for N 1s of NSSC-600 which is deconvoluted into four peaks of pyridinic-N, pyrrolic-N, graphitic-N, and oxidized-N at 398.2, 400.3, 401.3, and

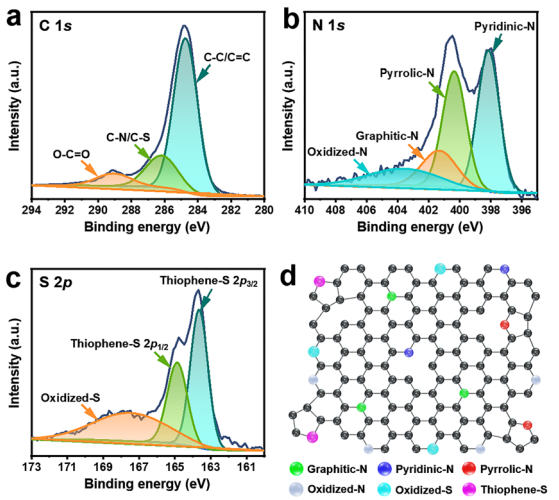

Fig. 3 High-resolution XPS for (a) C 1s, (b) N 1s, and (c) S 2p of NSSC-600. (d) Schematic description of identified bondings of heteroatoms (N and S) in the carbon matrix.

403.7 eV, respectively.[32,53] The N species of NSSC-600 is largely constituted of the pyridinic-N and the pyrrolic-N. Furthermore, the high-resolution XPS spectrum for S 2p of NSSC-600 is also provided with three deconvoluted peaks corresponding to the thiophene-S (163.6 eV and 164.9 eV) and oxidized-S (167.5 eV) (Fig. 3c). Fig. 3d schematically describes the identified bondings of N and S heteroatoms in the carbon matrix, which can serve as active sites for KIBs.

To assess the electrochemical behaviors, we first obtained the CV curves of SC and NSSC-*x* obtained at different temperatures (Fig. 4a and S5a–c†). The irreversible loss of CV areas between the first two cycles can be observed in the low voltage region for all samples due to the formation of a solid electrolyte interphase (SEI) layer and potential irreversible faradaic reactions.[54,55] The initial GCD curves of NSSC-400 demonstrate the lowest initial coulombic efficiency (ICE) of only 20% between the first and the second cycles among the samples (Fig. S5d and S6†). Such a great loss of irreversible initial capacity of NSSC-400 can be due to its low electrical conductivity obtained at such low carbonization temperature. In contrast, NSSC-*x* carbonized at temperatures at or above 600 °C show much higher ICE as compared to SC (Fig. S5e, f and S6†). Typically, NSSC-600 achieves the highest ICE of 60%, and it can be attributed to the optimal level of S and N dopants in the carbon matrix serving as additional surface redox-active sites, hence decreasing the portion of irreversible capacity generated on the surface. With the increase in treatment temperature, both NSSC-800 and NSSC-1000 show decreased ICE. Higher annealing temperatures potentially lead to changes in the microstructure of carbon materials, hence generating impurities and defects. These changes can influence the kinetics of electrochemical reactions in KIBs, thereby affecting the ICE. In addition, a much lower specific surface area of NSSC-600 (21 $m^2 g^{-1}$) than SC (272 $m^2 g^{-1}$) also limits the formation of the SEI layer on the surface, thus reducing the irreversible loss of initial capacity (Fig. S5†).[51] The initial discharge specific capacity of SC reaches 324 mA h g^{-1}, whereas the reversible specific capacity reaches 127 mA h g^{-1} at 100 mA g^{-1} from the second discharge. Among the NSSC-*x*, greater initial discharge specific capacity at 100 mA g^{-1} is achieved in the order of NSSC-400 (105 mA h g^{-1}), NSSC-1000 (323 mA g^{-1}), NSSC-600 (448 mA h g^{-1}), and NSSC-800 (492 mA h g^{-1}). However, due to the higher ICE of NSSC-600, it demonstrates the highest reversible specific capacity of 268 mA h g^{-1} among the samples. It is, therefore, concluded that NSSC-600 is the optimized anode material for KIBs in this study. Although the rate capability of NSSC-600 is slightly lower than that of SC potentially due to the presence of sluggish redox reactions of N and S heteroatoms, the capacity of NSSC-600 significantly outperforms that of SC at all current densities (Fig. 4c). Specifically, it is found that SC only presents the reversible specific capacities of 127, 93, 83, 66, and 57 mA h g^{-1} at 100, 200, 500, 1000, and 2000 mA g^{-1}, respectively. NSSC-600, in contrast, demonstrates a remarkable improvement in the electrochemical performance with the specific capacities of 268, 195, 168, 131, and 90 mA h g^{-1} at 100, 200, 500, 1000, and 2000 mA g^{-1}, respectively. Fig. S7† shows the cycling performance and CE of SC and NSSC-600 at 100 mA g^{-1}. SC only presents a reversible specific capacity of 94 mA h g^{-1} after 50 cycles. Compared with SC, NSSC-600 shows a significant electrochemical performance improvement, with a reversible specific capacity of 235 mA h g^{-1} after 50 cycles. To further evaluate SC and NSSC-600 as anode materials for KIBs, they were tested for their long-term cycling performance (Fig. 4d) and corresponding coulombic efficiency (CE) (Fig. S8†). NSSC-

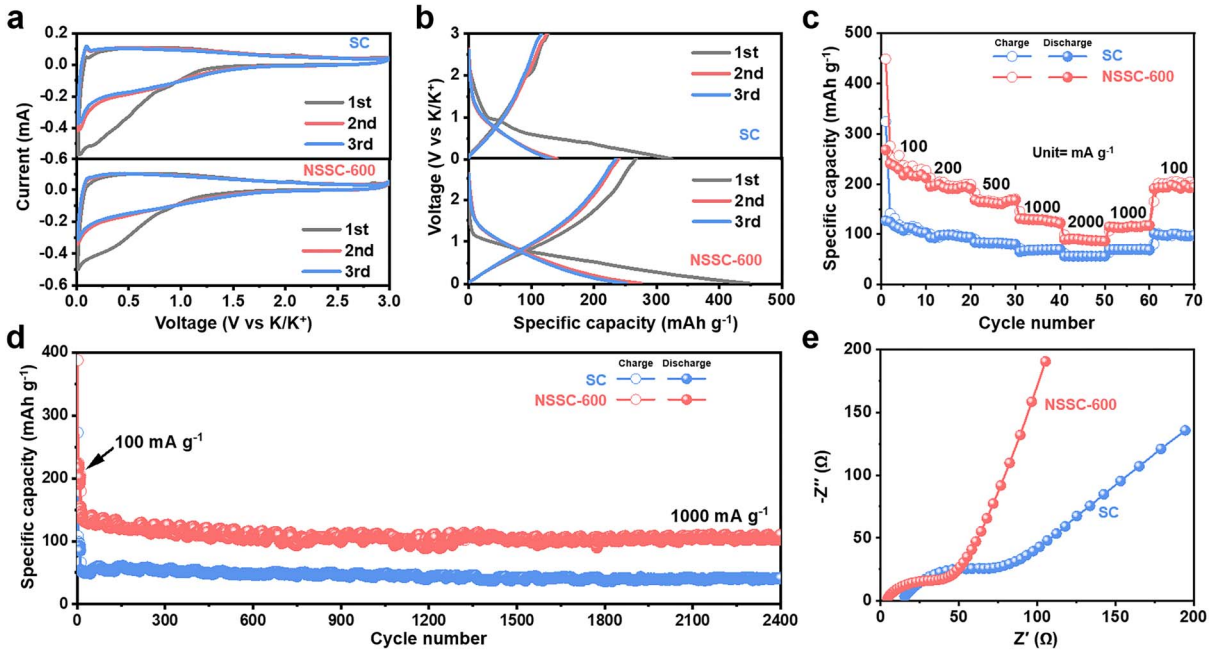

Fig. 4 (a) CV curves and (b) GCD curves of SC and NSSC-600. (c) Rate performance and (d) long-term cycling performance of SC and NSSC-600. (e) EIS of SC and NSSC-600.

600 achieves a high specific capacity of 110 mA h g^{-1} at 1000 mA g^{-1} after 2400 cycles, which is much higher than that of SC (41 mA h g^{-1} at 1000 mA g^{-1} after 2400 cycles). Although the performance of NSSC-600 is not the best as compared to the previously reported N, S co-doped carbons for KIBs, it is still considered to present an excellent performance among carbon materials derived from crop wastes (Tables S3 and S4†). Electrochemical impedance spectroscopy (EIS) was also conducted to gain more understanding of how electrode materials behave electrochemically in the half-cell (Fig. 4e). Compared with ionic diffusion, electron transfer capacity should play a dominant role in a battery system. Based on the fitted Nyquist plot, the decrease in the impedance involving electron transfer capacity is observed for NSSC-600, revealing that the N, S co-doping contributes to the enhancement of electron transfer, thus improving the K-ion storage performance.[56]

As N and S co-doping leads to obvious improvement in the K-ion storage capacity of anode materials in KIBs, we investigated the thermodynamic effect of N and S co-doping on intercalation by density functional theory (DFT) calculation. Typically, the adsorption energies and electronic structure of the four hypothetical carbons composed of carbon (C), S-doped carbon (C–S), N-doped carbon (C–N), and N, S co-doped carbon (S–C–S), respectively, were derived by the DFT calculations.[57] The corresponding calculation models are shown in Fig. 5a. According to the calculations with our proposed models, we found that the C, C–S, C–N, and S–C–S present the adsorption energy values of −1.89, −0.88, −2.24, and −2.42 eV, respectively (Fig. 5b). Generally, more negative adsorption energy indicates stronger adsorption capacity for K ions during the K-ion (de)intercalation processes, hence contributing to the enhancement of the K-ion storage performance.[58,59] According to the DFT calculations, the effect of C–N in the carbon matrix on reducing the energy required for K adsorption is found more significant than that of C–S. The S–C–N presents even less adsorption energy than C–N, suggesting that N and S have an integrative effect on reducing the energy for K adsorption. Fig. 5c shows the electronic localization function of C, C–S, C–N, and S–C–S after K adsorption. As compared to pristine C, it is found that heteroatom doping can influence the electronic structure of the carbon layer. The S–C–N incurs a greater net gain of electronic charge around N and S atoms in the carbon layer. This also suggests that the charge can be rapidly transferred from the N or S atom to the nearest neighboring carbon atom, which is consistent with the EIS result. Therefore, we believe that the N, S co-doping in carbon not only greatly improves the adsorption capacity of the K-ion but also accelerates the electron charge transfer, which are beneficial to the enhancement of K-ion storage.

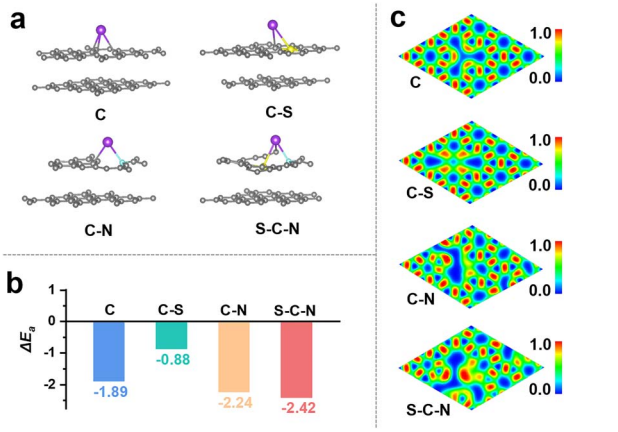

Fig. 5 DFT calculations: (a) the calculation models, (b) the adsorption energy, and (c) the electronic localization function of C, C–S, C–N, and S–C–N after K adsorption. The grey, yellow, cyan and violet balls indicate the C, S, N, and K atoms, respectively.

To further investigate the electrochemical properties, we performed *ex situ* Raman spectroscopy to identify the changes in the structure of NSSC-600 in different K-ion storage states (Fig. S9†). From Fig. S9b,† the I_D/I_G value of NSSC-600 gradually decreases during the discharge process as the surface of NSSC-600 tends to become more ordered in the K-ion insertion state. This is due to the reduced vibration in the presence of the adsorbed K-ions, hence resulting in a decrease in vibration intensity and a limited sp^2 breathing motion of carbon. However, with the deintercalation of K-ions, the I_D/I_G value is recovered to a certain level, but still deviates from the value of its pristine state because some adsorbed K-ions are irreversibly trapped in the carbon matrix. In addition, we also performed an *ex situ* FTIR to study the evolution of NSSC-600 in different charge–discharge states (Fig. S9c†). As compared to the pristine state, only weak $\nu_{(C^-K)}$ vibrational peaks are observed upon discharging to 0.8 V, indicating the adsorption state of K-ions. When discharged to 0.01 V, a very strong $\nu_{(C^-K)}$ vibrational peak is observed, indicating an effective K-ion intercalation. In the subsequent charging stage, the $\nu_{(C^-K)}$ vibrational peak gradually weakens, demonstrating a good reversibility of K-ion (de)intercalation processes in NSSC-600. The FESEM images of NSSC-600 after 50 cycles show that the nanosheet-like structure is largely maintained with no visible cracking phenomenon in the electrode at the macroscopic level (Fig. S10a and b†). In the TEM and high-resolution TEM images of NSSC-600 after 50 cycles, a disordered carbon microstructure is still observed with a certain level of orderliness in the carbon lattice (Fig. S10c and d†). The Raman spectra of NSSC-600 before and after 50 cycles are also presented in Fig. S11.† It is found that the I_D/I_G ratio of NSSC-600 increases from 0.93 in pristine to 1.01 after 50 cycles, indicating that there is a certain effect on the graphitization of NSSC-600 by potassiation–depotassiation processes. This is speculated to be due to the insertion of potassium ions into the interlayer or gap after multiple charge and discharge cycles, which causes the disordered carbon layers to rearrange at specific interlayer distances.

As K-ion storage in hard carbon anode materials occurs by both diffusion-controlled and capacitive mechanisms, it is important to understand how each mechanism contributes to the overall capacity. We, therefore, differentiated the contributions of two different mechanisms from the CV curves of SC and NSSC-600 at the scan rate from 0.2 to 1.2 mV s^{-1} (Fig. 6a and b). It is found that both electrodes present similar shapes at different scan rates, indicating that they exhibit similar K-ion

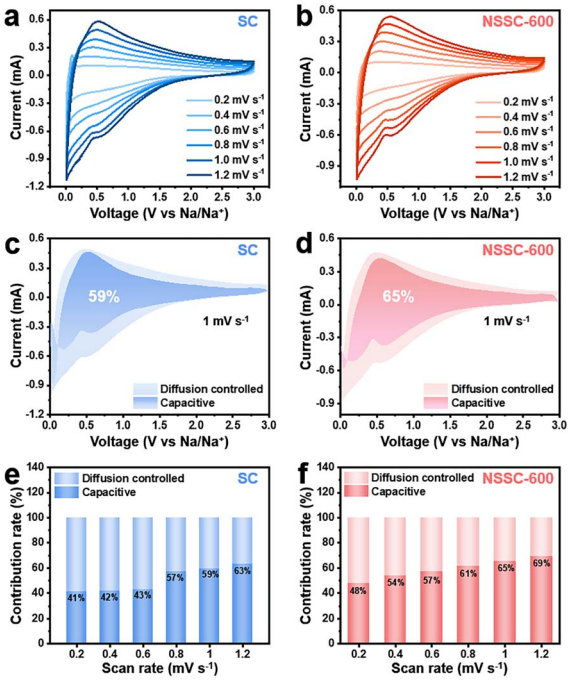

Fig. 6 CV curves of (a) SC and (b) NSSC-600 at the scan rates from 0.2 to 1.2 mV s^{-1}. Capacitive contribution area of (c) SC and (d) NSSC-600 at 1.0 mV s^{-1}. Capacitive contribution ratios of (e) SC and (f) NSSC-600 at the scan rates from 0.2 to 1.2 mV s^{-1}.

storage electrochemical behaviors. The capacitive contributions were calculated based on eqn (1):[60,61]

$$i(V) = k_1 v + k_2 v^{1/2} \quad (1)$$

Eqn (1) can be converted to eqn (2):

$$i(V)/v^{1/2} = k_1 v^{1/2} + k_2 \quad (2)$$

In eqn (2), $k_1 v$ and $k_2 v^{1/2}$ represent the capacitive and diffusion-controlled behaviors for K-ion storage, respectively. From the calculation, it is found that SC exhibits a capacitive contribution of 59% at 1.0 mV s^{-1} (Fig. 6c), and it is improved to 65% for NSSC-600 (Fig. 6d). The capacitive contributions of SC and NSSC-600 from 0.2 to 1.2 mV s^{-1} are shown in Fig. 6e and f. The capacitive contributions of SC are 41, 42, 43, 57, 59 and 63% at 0.2, 0.4, 0.6, 0.8, 1.0 and 1.2 mV s^{-1}, respectively. NSSC-600 demonstrates increased capacitive contributions of 48, 54, 57, 61, 65 and 69% at the scan rates of 0.2, 0.4, 0.6, 0.8, 1.0 and 1.2 mV s^{-1}, respectively. Considering that the synthesis of NSSC-600 is mainly derived from the surface reaction, the doped S and N species mainly exist on the surface of NSSC-600. Such surface doping of carbon by S and N contributes to capacitive behavior, therefore allowing the rapid K-ion storage.

Conclusion

In our work, we present the mechanical nanoarchitecturing of sorghum biomass to obtain nanosheet-like morphology, and its N and S co-doped porous carbon (NSSC) upon direct-carbonization with thiourea as the source of N and S dopants. As-synthesized NSSC-600 successfully demonstrates a great enhancement of K-ion storage performance with a high reversible specific capacity of 268 mA h g^{-1} at 100 mA g^{-1}, and an ultra-stable reversible specific capacity of 110 mA h g^{-1} even after 2400 cycles at a high current density of 1 A g^{-1}. The DFT calculation elucidates the thermodynamic effect of the N, S co-doping in carbon to remarkably reduce the adsorption energy of K, hence improving the K-ion adsorption behavior and accelerating the charge transfer during the K-ion (de)intercalation processes. This work, therefore, presents a facile and cost-effective synthetic method to obtain a nanosheet-like N, S co-doped carbon for use as a high-performance anode material in KIBs.

Author contributions

M. K., L. M. and R. A. A. conducted the experiments. M. K. and L. M. wrote the manuscript. M. K., Z. L., W. M. and R. A. A. characterized the materials. N. A., A. R., A. Q., D. M and Y. Y. revised the manuscript. A. K. N., J. L. and Y. Y. conceptualized.

Conflicts of interest

There are no conflicts to declare.

Acknowledgements

This research was supported by Fundamental Research Funds for the Central Universities (21621406) and Science and Technology Program of Guangzhou, China (202102020737 and 201605030008), the JST-ERATO Yamauchi Materials Space-Tectonics Project, Japan (JPMJER2003) and the Australian Research Council (ARC) through a Linkage Project, Australia (LP180100429). This work was performed in part at the Queensland node of the Australian National Fabrication Facility, a company established under the National Collaborative Research Infrastructure Strategy to provide nano and microfabrication facilities for Australia's researchers. We are also grateful to NIT Corporation for the support in the discussion of the battery system.

References

1 F. Wu, J. Maier and Y. Yu, *Chem. Soc. Rev.*, 2020, **49**, 1569–1614.
2 M. Li, J. Lu, X. Ji, Y. Li, Y. Shao, Z. Chen, C. Zhong and K. Amine, *Nat. Rev. Mater.*, 2020, **5**, 276–294.
3 H. P. Jia, X. L. Li, J. H. Song, X. Zhang, L. L. Luo, Y. He, B. S. Li, Y. Cai, S. Y. Hu, X. C. Xiao, C. M. Wang, K. M. Rosso, R. Yi, R. Patel and J. G. Zhang, *Nat. Commun.*, 2020, **11**, 1474.
4 M. Kim, J. F. S. Fernando, J. Wang, A. K. Nanjundan, J. Na, M. S. A. Hossain, H. Nara, D. Martin, Y. Sugahara, D. Golberg and Y. Yamauchi, *Chem. Commun.*, 2022, **58**, 863–866.

5 J. Xie, J. Li, X. Li, H. Lei, W. Zhuo, X. Li, G. Hong, K. N. Hui, L. Pan and W. Mai, *CCS Chem.*, 2021, **3**, 791–799.
6 Y. Lan, W. Yao, X. He, T. Song and Y. Tang, *Angew. Chem., Int. Ed.*, 2020, **59**, 9255–9262.
7 H. Li, X. Zhang, Z. Zhao, Z. Hu, X. Liu and G. Yu, *Energy Storage Mater.*, 2020, **26**, 83–104.
8 W. Zhuo, J. Li, X. Li, L. Ma, G. Yan, H. Wang, S. Tan and W. Mai, *Surf. Interface*, 2021, **23**, 100911.
9 Y. Zhang, J. Li, L. Ma, H. Li, X. Xu, X. Liu, T. Lu and L. Pan, *Chem. Eng. J.*, 2022, **427**, 130936.
10 C. Hakim, N. Sabi and I. Saadoune, *J. Energy Chem.*, 2021, **61**, 47–60.
11 J. Park, Y. Shim, Y. Kim, Y. Choi, H. Lee, J. Park, J. Wang, Y. Lee, J. Chang, K. Yim, C. Ahn, C. Lee, K. Kim and J. Yuk, *J. Mater. Chem. A*, 2020, **8**, 20436–20445.
12 Y. Dong, J. Xu, M. Chen, Y. Guo, G. Zhou, N. Li, S. Zhou and C. Wong, *Nano Energy*, 2020, **68**, 104357.
13 J. Xie, X. Li, H. Lai, Z. Zhao, J. Li, W. Zhang, W. Xie, Y. Liu and W. Mai, *Angew. Chem., Int. Ed.*, 2019, **58**, 14740–14747.
14 Y. Feng, M. Xu, T. He, B. Chen, F. Gu, L. Zu, R. Meng and J. Yang, *Adv. Mater.*, 2021, **33**, 2007262.
15 X. Li, J. Li, W. Zhuo, Z. Li, L. Ma, Z. Ji, L. Pan and W. Mai, *Nano-Micro Lett.*, 2021, **13**, 179.
16 C. Huang, A. Xu, G. Li, H. Sun, S. Wu, Z. Xu and Y. Yan, *Small*, 2021, **17**, 2100685.
17 H. Liang, Y. Zhang, S. Hao, L. Cao, Y. Li, Q. Li, D. Chen, X. Wang, X. Guo and H. Li, *Energy Storage Mater.*, 2021, **40**, 250–258.
18 J. Wu, S. Liu, Y. Rehman, T. Huang, J. Zhao, Q. Gu, J. Mao and Z. Guo, *Adv. Funct. Mater.*, 2021, **31**, 2010832.
19 E. Li, L. Ma, Z. Li, H. Wang, G. Zhang, S. Li, J. Li, L. Pan, W. Mai and J. Li, *Nanoscale*, 2022, **14**, 11179–11186.
20 J. Liu, X. Yu, J. Bao, C.-F. Sun and Y. Li, *J. Phys. Chem. Solids*, 2021, **153**, 109992.
21 J. Duan, D. Zou, J. Li, J. Weng, Y. Liu, S. Gong, A. Li and P. Zhou, *Electrochim. Acta*, 2021, **376**, 138047.
22 J. Cao, J. Zhong, H. Xu, S. Li, H. Deng, T. Wang, L. Fan, X. Wang, L. Wang, J. Zhu, B. Lu and X. Duan, *Nano Res.*, 2022, **15**, 2040–2046.
23 H. Ma, X. Qi, D. Peng, Y. Chen, D. Wei, Z. Ju and Q. Zhuang, *ChemistrySelect*, 2019, **4**, 11488–11495.
24 W. Yang, J. Zhou, S. Wang, Z. Wang, F. Lv, W. Zhang, W. Zhang, Q. Sun and S. Guo, *ACS Energy Lett.*, 2020, **5**, 1653–1661.
25 G. Zhao, D. Yu, H. Zhang, F. Sun, J. Li, L. Zhu, L. Sun, M. Yu, F. Besenbacher and Y. Sun, *Nano Energy*, 2020, **67**, 104219.
26 X. Yuan, B. Zhu, J. Feng, C. Wang, X. Cai and R. Qin, *Chem. Eng. J.*, 2021, **405**, 126897.
27 M. Kim, J. F. S. Fernando, Z. Li, A. Alowasheeir, A. Ashok, R. Xin, D. Martin, A. Kumar Nanjundan, D. V. Golberg, Y. Yamauchi, N. Amiralian and J. Li, *Chem. Eng. J.*, 2022, **445**, 136344.
28 W.-j. Deng, X.-d. He, L.-m. Zhang, J.-r. Wang and C.-h. Chen, *Energy Technol.*, 2021, **9**, 2100644.
29 W. Cao, E. Zhang, J. Wang, Z. Liu, J. Ge, X. Yu, H. Yang and B. Lu, *Electrochim. Acta*, 2019, **293**, 364–370.
30 W. Y. Chen, D. H. Xu, S. J. Kuang, Z. Q. Wu, H. Hu, M. T. Zheng and X. Y. Yu, *J. Power Sources*, 2021, **489**, 229459.
31 A. Mehmood, G. Ali, B. Koyuturk, J. Pampel, K. Chung and T. Fellinger, *Energy Storage Mater.*, 2020, **28**, 101–111.
32 L. Ma, Z. B. Li, J. L. Li, Y. Dai, C. Qian, Y. F. Zhu, H. Wang, K. N. Hui, L. K. Pan, M. A. Amin, Y. Yamauchi and W. J. Mai, *J. Mater. Chem. A*, 2021, **9**, 25445–25452.
33 Y. Li, M. Chen, B. Liu, Y. Zhang, X. Liang and X. H. Xia, *Adv. Energy Mater.*, 2020, **10**, 2000927.
34 A. Hosseinmardi, P. K. Annamalai, B. Martine, J. Pennells, D. J. Martin and N. Amiralian, *ACS Omega*, 2018, **3**, 15933–15942.
35 B. Mu, H. Wang, X. Hao and Q. Wang, *Polymers*, 2018, **10**, 1–15.
36 Y. Xu, S. Liu, M. Wang, J. Zhang, H. Ding, Y. Song, Y. Zhu, Q. Pan, C. Zhao and H. Deng, *J. Hazard. Mater.*, 2021, **416**, 125796.
37 M. Chen, T. H. Le, Y. X. Zhou, F. Y. Kang and Y. Yang, *ACS Appl. Energy Mater.*, 2020, **3**, 1653–1664.
38 F. Wu, M. H. Zhang, Y. Bai, X. R. Wang, R. Q. Dong and C. Wu, *ACS Appl. Mater. Interfaces*, 2019, **11**, 12554–12561.
39 X. H. Tan, K. R. Jiang, S. L. Zhai, J. G. Zhou, J. Wang, K. Cadien and Z. Li, *Small*, 2021, **17**, 2102109.
40 K. Wang, Y. B. Xu, Y. Li, V. Dravid, J. S. Wu and Y. Huang, *J. Mater. Chem. A*, 2019, **7**, 3327–3335.
41 M. Kim, K. L. Firestein, J. F. Fernando, X. Xu, H. Lim, D. V. Golberg, J. Na, J. Kim, H. Nara and J. Tang, *Chem. Sci.*, 2022, **13**, 10836–10845.
42 X. D. Li, Z. B. Liu, J. L. Li, H. Lei, W. C. Zhuo, W. Qin, X. Cai, K. N. Hui, L. K. Pan and W. J. Mai, *J. Energy Chem.*, 2021, **53**, 56–62.
43 M. Kim, X. Xu, R. Xin, J. Earnshaw, A. Ashok, J. Kim, T. Park, A. K. Nanjundan, W. A. El-Said, J. W. Yi, J. Na and Y. Yamauchi, *ACS Appl. Mater. Interfaces*, 2021, **13**, 52034–52043.
44 J. X. Hu, Y. Y. Xie, M. Yin and Z. A. Zhang, *J. Energy Chem.*, 2020, **49**, 327–334.
45 X. Zhao, Y. Ding, Q. Xu, X. Yu, Y. Liu and H. Shen, *Adv. Energy Mater.*, 2019, **9**, 1803648.
46 V.-T. Hoang, X.-D. Ngo, N. Le Nhat Trang, D. Thi Nguyet Nga, N. T. Khi, V. T. Trang, V. D. Lam and A.-T. Le, *Colloids Surf., A*, 2022, **636**, 128165.
47 M. Mariappan, G. Madhurambal, B. Ravindran and S. C. Mojumdar, *J. Therm. Anal. Calorim.*, 2011, **104**, 915–921.
48 X. Rao, Y. Lou, J. Chen, H. Lu, B. Cheng, W. Wang, H. Fang, H. Li and S. Zhong, *Front. Energy Res.*, 2020, **8**, 1–9.
49 M. He, K. Kraychyk, M. Walter and M. Kovalenko, *Nano Lett.*, 2014, **14**, 1255–1262.
50 Z. Hong, Y. Zhen, Y. Ruan, M. Kang, K. Zhou, J. M. Zhang, Z. Huang and M. Wei, *Adv. Mater.*, 2018, **30**, 1802035.
51 L. Tao, Y. Yang, H. Wang, Y. Zheng, H. Hao, W. Song, J. Shi, M. Huang and D. Mitlin, *Energy Storage Mater.*, 2020, **27**, 212–225.
52 J. Li, W. Qin, J. Xie, H. Lei, Y. Zhu, W. Huang, X. Xu, Z. Zhao and W. Mai, *Nano Energy*, 2018, **53**, 415–424.

53 M. Kim, T. Park, C. Wang, J. Tang, H. Lim, M. S. A. Hossain, M. Konarova, J. W. Yi, J. Na, J. Kim and Y. Yamauchi, *ACS Appl. Mater. Interfaces*, 2020, **12**, 34065–34073.
54 H. W. Wang, D. Y. Zhai and F. Y. Kang, *Energy Environ. Sci.*, 2020, **13**, 4583–4608.
55 N. Takenaka, A. Bouibes, Y. Yamada, M. Nagaoka and A. Yamada, *Adv. Mater.*, 2021, **33**, 2100574.
56 S. Men, J. J. Lin, Y. Zhou and X. W. Kang, *J. Power Sources*, 2021, **485**, 229310.
57 J. Li, N. Zhuang, J. Xie, X. Li, W. Zhuo, H. Wang, J. B. Na, X. Li, Y. Yamauchi and W. Mai, *Adv. Energy Mater.*, 2020, **10**, 1903455.
58 Y. Xu, X. Sun, Z. Li, L. Wei, G. Yao, H. Niu, Y. Yang, F. Zheng and Q. Chen, *Nanoscale*, 2021, **13**, 19634–19641.
59 C. Chen, Z. Wang, B. Zhang, L. Miao, J. Cai, L. Peng, Y. Huang, J. Jiang, Y. Huang and L. Zhang, *Energy Storage Mater.*, 2017, **8**, 161–168.
60 K. Ma, Y. Liu, H. Jiang, Y. Hu, R. Si, H. Liu and C. Li, *CCS Chem.*, 2021, **3**, 1472–1482.
61 Z. Wang, C. Duan, D. Wang, K. Dong, S. Luo, Y. Liu, Q. Wang, Y. Zhang and A. Hao, *J. Colloid Interface Sci.*, 2020, **580**, 429–438.